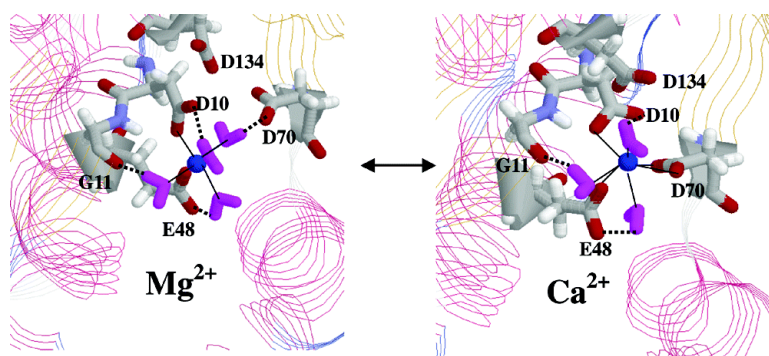Article

A Combined Experimental and Theoretical Study of Divalent Metal Ion Selectivity and Function in Proteins: Application to *E. coli* Ribonuclease H1

C. Satheesan Babu, Todor Dudev, R. Casareno, J. A. Cowan, and Carmay Lim

More About This Article

Additional resources and features associated with this article are available within the HTML version:

- Supporting Information
- Links to the 5 articles that cite this article, as of the time of this article download
- Access to high resolution figures
- Links to articles and content related to this article
- Copyright permission to reproduce figures and/or text from this article

View the Full Text HTML

A Combined Experimental and Theoretical Study of Divalent Metal Ion Selectivity and Function in Proteins: Application to *E. coli* Ribonuclease H1

C. Satheesan Babu,[†] Todor Dudev,[†] R. Casareno,[‡] J. A. Cowan,[‡] and
Carmay Lim*,[†,§]

*Contribution from the Institute of Biomedical Sciences, Academia Sinica,
Taipei 11529, Taiwan, R.O.C., Department of Chemistry, The Ohio State University,
100 West 18th Avenue, Columbus, Ohio 43210, and Department of Chemistry,
National Tsing Hua University, Hsinchu 300, Taiwan, R.O.C.*

Received March 3, 2003; E-mail: carmay@gate.sinica.edu.tw

Abstract: Structural and thermodynamic aspects of alkaline earth metal dication (Mg^{2+}, Ca^{2+}, Sr^{2+}, Ba^{2+}) binding to *E. coli* ribonuclease H1 (RNase H1) have been investigated using both experimental and theoretical methods. The various metal-binding modes of the enzyme were explored using classical molecular dynamics simulations, and relative binding free energies were subsequently evaluated by free energy simulations. The trends in the free energies of model systems based on the simulation structures were subsequently verified using a combination of density functional theory and continuum dielectric methods. The calculations provide a physical basis for the experimental results and suggest plausible role-(s) for the metal cation and the catalytically important acidic residues in protein function. Magnesium ion indirectly activates water attack of the phosphorus atom by freeing one of the active site carboxylate residues, D70, to act as a general base through its four first-shell water molecules, which prevent D70 from binding directly to Mg^{2+}. Calcium ion, on the other hand, inhibits enzyme activity by preventing D70 from acting as a general base through bidentate interactions with both carboxylate oxygen atoms of D70. These additional interactions to D70, in addition to the D10 and E48 monodentate interactions found for Mg^{2+}, enable Ca^{2+} to bind tighter than the other divalent ions. However, a bare Mg^{2+} ion with two or less water molecules in the first shell could bind directly to the three active-site carboxylates, in particular D70, thus inhibiting enzymatic activity. The present analyses and results could be generalized to other members of the RNase H family that possess the same structural fold and show similar metal-binding site and Mg^{2+}-dependent activity.

Introduction

Divalent metal cations, such as Zn^{2+}, Mg^{2+}, and Ca^{2+}, are often associated with catalytic or regulatory activities of proteins that constitute some of the fundamental chemical life processes.[1-3] Yet, the mechanisms by which a metal ion is selected by a protein and subsequently regulates protein function are generally not well understood. A detailed knowledge of these two issues could provide guidelines to the design of potent inhibitors or drug molecules for certain metalloproteins. Furthermore, sequence motif and preferences of first and higher coordination shells of amino acid side chains around each metal ion could help to engineer metal-binding sites and/or design novel ones.[4-6]

To elucidate how a protein selects a specific metal ion and the role of the ion in protein function, we have chosen to study the enzyme *Escherichia coli* ribonuclease H1 (RNase H1), which catalyzes the hydrolysis of the RNA strand of a RNA.DNA hybrid to yield a 3′-hydroxyl and a 5′-phosphate in a divalent cation-dependent manner.[7,8] This protein provides a good model system to study the binding of divalent cations and the subsequent role in catalysis for the following three reasons. First, RNase H1 belongs to the superfamily of polynucleotide transferases, including resolvase, integrase, transposase, and exonuclease III, that have homologous active sites and metal-dependent nucleic acid-modifying functions;[9,10] thus, the analyses and results in this work could be generalized to other members in this family. Second, the RNase H domain of HIV reverse transcriptase is needed to reverse transcribe the viral single-stranded RNA genome into double-stranded DNA for integration into the host chromosome;[1] thus, it is a potential target for anti-

[†] Academia Sinica.
[‡] The Ohio State University.
[§] National Tsing Hua University.
(1) Stryer, L. *Biochemistry*, 4th ed.; W. H. Freeman and Co.: New York, 1995.
(2) Nicholson, A. W. *Ribonucleases: Structures and functions*; D'Alessio, G., Riordan, J. F., Eds.; Academic Press: San Diego, 1997.
(3) Cowan, J. A. *Chem. Rev.* **1998**, *98*, 1067.
(4) Jernigan, R.; Raghunathan, G.; Bahar, I. *Curr. Opin. Struct. Biol.* **1994**, *4*, 256.
(5) Lu, Y.; Valentine, J. S. *Curr. Opin. Struct. Biol.* **1997**, *7*, 495.
(6) Lu, Y.; Berry, S. M.; Pfister, T. D. *Chem. Rev.* **2001**, *101*, 3047.

(7) Crouch, R. J. *New Biol.* **1990**, *2*, 771.
(8) Hostomsky, Z.; Hostomska, Z.; Matthews, D. A., Eds. *Nucleases*; Cold Spring Harbor Laboratory: Cold Spring Harbor, NY, 1994.
(9) Yang, W.; Steitz, T. A. *Structure* **1995**, *3*, 131.
(10) Venclovas, C.; Siksnys, V. *Nat. Struct. Biol.* **1995**, *2*, 838.

Figure 1. Crystal structure (2.8 Å) of Mg^{2+}-bound *E. coli* ribonuclease H1 (PDB entry 1RDD). The Mg^{2+} ion is in blue, while its protein ligands, i.e., the G11 backbone O and D10 and E48 carboxyl O, are in red. The positions of D70 and D134 are also shown.

HIV therapy. Third, RNase H1 is well characterized both structurally and thermodynamically. There are two high-resolution X-ray structures of metal-free RNase H1,[11,12] X-ray structures of the Mg^{2+}-[13] and Mn^{2+}-bound[14] enzyme, and X-ray structures of several active-site mutants.[15] The charge states of most of the histidines and all of the acidic residues in the free enzyme have been determined.[16,17] Moreover, the free energies and entropies of Mg^{2+}, Mn^{2+}, and Ca^{2+} dications binding to RNase H1 have been measured.[18]

Based on the X-ray structures and site-directed mutagenesis experiments, the active-site residues responsible for metal binding and enzymatic activity have been identified.[19−21] The invariant D10 and E48 side chains as well as the G11 backbone are involved in Mg^{2+} binding (Figure 1). In particular, the D10 side chain appears to be essential for Mg^{2+} binding as the D10A mutant cannot bind to Mg^{2+}.[22−24] The two Mg^{2+} ligands, D10 and E48, as well as D70 are required for enzyme activity. With Mg^{2+} as a cofactor for activity, D70 has been proposed to act as a general base by deprotonating a water nucleophile for subsequent phosphate attack, whereas a Mg^{2+}-bound water molecule acts as a general acid by donating a proton to the departing O3′ oxygen of the RNA.[13,16,19,25−28] However, E48

and H124 have also been proposed to be the nucleophile-producing general base; hence, the identity of the general base remains an open question.

Despite the wealth of experimental data accumulated on RNase H1, several questions, particularly on the mode of metal binding and its role in modulating enzyme activity, remain. RNase H1 requires divalent cations for its catalytic activity.[7] Apparently, only one metal ion is required for catalysis,[29] as the enzyme binds to metal ions in a 1:1 stoichiometry and the X-ray structure of Mg^{2+}-bound RNase H1 shows only one binding site.[13] However, it is not clear why RNase H1 is fully active in the presence of Mg^{2+} and Mn^{2+} ions,[14,18,30] but shows negligible activity with Ca^{2+} and practically zero activity for even larger ions such as Sr^{2+} and Ba^{2+}.[18] Another intriguing question is how the enzyme selects Mg^{2+} over Ca^{2+} when it binds Ca^{2+} tighter than Mg^{2+} (by 2.2 kcal/mol), and why it is inactive with Ca^{2+} but active with Mg^{2+}.[18] One possibility is that Ca^{2+} binds to D70, in addition to the Mg^{2+} protein ligands, D10, G11, and E48. The additional interactions between Ca^{2+} and D70 would allow Ca^{2+} to bind tighter than Mg^{2+} but, at the same time, inhibit enzymatic activity if D70 acts as a general base in RNase H1 catalysis, as proposed in previous work.[18]

To test this hypothesis and to elucidate the effects of solvent and coordination mode (bidentate vs monodentate) upon metal binding, as well as the specific roles of amino acid ligands in metal ion selectivity, we undertook a combined experimental and theoretical investigation of the series of alkaline earth metal dications (Mg^{2+}, Ca^{2+}, Sr^{2+}, and Ba^{2+}) binding to RNase H1 in solution. First, the binding free energies, enthalpies, and entropies of the alkaline earth metal dications were measured. The plausible metal-binding site conformations were obtained from molecular dynamics (MD) simulations using ion−water/ protein force fields developed in our previous work.[31] Based on these structures, relative binding free energies were derived from free energy simulations using a thermodynamic integration approach. Because electronic effects, such as charge transfer from the ligands to the metal, play a crucial role in determining the metal complex properties[32,33] but are not explicitly considered in the classical simulations, the key simulation results were verified by computing the free energies for exchanging the native cofactor, Mg^{2+}, for Ca^{2+} in model binding sites using density functional theory (DFT) combined with continuum dielectric method (CDM). The amino acid residues found coordinated directly or indirectly to the metal in RNase H1 were modeled by simple organic molecules, which together with the metal were treated quantum mechanically, while the rest of the protein was treated as a dielectric continuum. The theoretical results in conjunction with available experimental data suggest plausible binding modes of the dications and how they affect catalytic activity.

Methods

Experiments. I. Bacterial Growth and Enzyme Purification. Recombinant native and mutant ribonuclease H1 were overexpressed in *E. coli* BL21 (DE3) following IPTG induction. Growth conditions

(11) Katayanagi, K.; Miyagawa, M.; Matsushima, M.; Ishikawa, S.; Kanaya, S.; Ikehara, M.; Matsuzaki, T.; Morikawa, K. *Nature* **1990**, *347*, 306.
(12) Yang, W.; Hendrickson, W. A.; Crouch, R. J.; Satow, Y. *Science* **1990**, *249*, 1398.
(13) Katayanagi, K.; Ishikawa, M.; Morikawa, K. *Proteins: Struct., Funct., Genet.* **1993**, *17*, 337.
(14) Goedken, E. R.; Marqusee, S. *J. Biol. Chem.* **2001**, *276*, 7266.
(15) Katayanagi, K.; Ishikawa, S.; Okumura, M.; Ariyoshi, M.; Kanaya, S.; Kawano, Y.; Suzuki, M.; Tanaka, I.; Morikawa, K. *J. Biol. Chem.* **1993**, *2683*, 22092.
(16) Oda, Y.; Yoshida, M.; Kanaya, S. *J. Biol. Chem.* **1993**, *268*, 88.
(17) Oda, Y.; Yamazaki, T.; Nagayama, K.; Kanaya, S.; Kuroda, Y.; Nakamura, H. *Biochemistry* **1994**, *33*, 5275.
(18) Casareno, R. L. B.; Cowan, J. A. *Chem. Commun.* **1996**, 1813.
(19) Kanaya, S.; Kohara, A.; Miura, Y.; Sekiguchi, A.; Iwai, S.; Inoue, H.; Ohtsuka, E.; Ikehara, M. *J. Biol. Chem.* **1990**, *265*, 4615.
(20) Kanaya, S.; Katsuda-Nakai, C.; Ikehara, M. *J. Biol. Chem.* **1991**, *226*, 11621.
(21) Kanaya, S.; Katayanagi, K.; Inoue, H.; Ohtsuka, E.; Ikehara, M. *Eur. J. Biochem.* **1991**, *198*, 437.
(22) Kanaya, S.; Oobatake, M.; Liu, Y. *J. Biol. Chem.* **1996**, *271*, 32729.
(23) Rashke, T. M.; Marqusee, S. *Nat. Struct. Biol.* **1997**, *4*, 298.
(24) Goedken, E. R.; Keck, J. L.; Berger, J. M.; Marqusee, S. *Protein Sci.* **2000**, *9*, 1914.
(25) Oda, Y.; Nakamura, H.; Kanaya, S.; Ikehara, M. *J. Biomol. NMR* **1991**, *1*, 274.
(26) Haruki, M.; Noguchi, E.; Nakai, C.; Liu, Y. Y.; Oobatake, M.; Itaya, M.; Kanaya, S. *Eur. J. Biochem.* **1994**, *220*, 623.
(27) Huang, H.-W.; Cowan, J. A. *Eur. J. Biochem.* **1994**, *198*, 4437.

(28) Casareno, R. L. B.; Li, D.; Cowan, J. A. *J. Am. Chem. Soc.* **1995**, *117*, 11011.
(29) Black, C. B.; Huang, H. W.; Cowan, J. A. *Coord. Chem. Rev.* **1994**, *135/136*, 165.
(30) Keck, J. L.; Goedken, E. R.; Marqusee, S. *J. Biol. Chem.* **1998**, *273*, 34128.
(31) Babu, C. S.; Lim, C. In preparation.
(32) Dudev, T.; Lim, C. *J. Phys. Chem. A* **1999**, *103*, 8093.
(33) Dudev, T.; Lim, C. *J. Am. Chem. Soc.* **2000**, *122*, 11146.

ion	ϵ^a (kcal/mol)	R_{min}^b (Å)
Mg^{2+}	0.315 88	2.6440
Ca^{2+}	0.091 55	3.3734
Sr^{2+}	0.073 38	3.6957
Ba^{2+}	0.084 64	3.9282

^{a} The well depth of the vdW interaction energy between the ion and water molecules. ^{b} The distance between the ion and the water oxygen corresponding to the position of ϵ.

for *E. coli* and protein purification protocols have been described elsewhere.[18] The recombinant native RNase H1 was purified using a nickel affinity column according to the Novagen protocol with minor modifications. The bound protein was eluted from the column using 85−95 mM histidine. SDS protein gels stained with Coomassie blue confirmed the purity of enzyme samples. Samples for calorimetry experiments were dialyzed extensively in 20 mM Tris pH 7.0 and 1 mM 2-mercaptoethanol at 4 °C for at least 36 h immediately before use.

II. Calorimetric Measurements. Data were collected on a Microcal OMEGA ultrasensitive titration calorimeter (MicroCal Inc.). From 20 to 25 injections of 10 to 12.5 μL volumes of divalent metal (2 to 5 mM) were delivered into the reaction cell (1.3415 mL) containing 0.1−0.2 mM enzyme at 298 K. Each injection was delivered over a 10 s time interval, with a 5 to 10 min interval between injections to allow for complete equilibration. Background buffer was the same for all solutions (20 mM Tris, pH 7.5, 1 mM 2-mercaptoethanol) to minimize the heat changes from mixing. Control experiments in the absence of enzyme were used to determine and, if necessary, correct for background heats of dilution. In all cases studied here, all parameters were floating during data fit.

MD Simulations. I. Protonation States. MD simulations using the program CHARMM27[34] were carried out on fully solvated RNase HI consisting of 2459 protein atoms and 5072 TIP3P[35] water molecules at a mean temperature of 300 K and at neutral pH, the pH at which the experiments were performed. The measured pK_a values of all carboxyl groups[17] and histidines[16] indicate that, at pH 7, the aspartic and glutamic acids would be deprotonated, while the histidines would be protonated except for H83 ($pK_a = 5.5$) and H114 ($pK_a = 5.0$), which are deprotonated. The imidazole nitrogen atoms of H83 and H114 are ≥25 and ≥22 Å, respectively, from the Mg^{2+} ion in the X-ray structure. The pK_a values of the other ionizable groups in RNase HI have not been measured and are assumed to be normal: thus, all lysines and arginines are positively charged.

II. Force Field. The MD simulations employed the all-hydrogen CHARMM22 force field,[36] the TIP3P[35] water model, and periodic boundary conditions with a truncated octahedral primary simulation box. The ion−water interaction energies were modeled by a sum of Coulomb and van der Waals pairwise energies using parameters derived in our previous work (see Table 1).[31] These parameters were constructed so as to reproduce the experimental first and second-shell ion−water distances, coordination numbers, and solvation free energies[37] (see Results below). They were then used in conjunction with traditional combining rules for ion−protein interactions in the simulations below. All the hydrogen atoms were constrained during the simulations

using the SHAKE algorithm.[38] The nonbonded interactions were truncated at 13 Å using a force-switching function in the region from 10 to 12 Å.

III. Simulation Protocol. The starting point for the simulation of Mg^{2+}-bound RNase H1 was the X-ray structure of the Mg^{2+}-bound protein (PDB entry 1RDD, Figure 1), to which hydrogen atoms were added. The resulting structure was energy minimized with strong harmonic constraints on all heavy atoms to remove bad contacts. Next, the structure was immersed at the center of a previously equilibrated truncated octahedral box (of cubic edge length 70 Å) of TIP3P water molecules, and its orientation in the primary box was optimized so as to ensure sufficient solvation of all parts of the protein.[39] Water molecules whose oxygen atoms were within 2 Å of any protein heavy atoms were deleted. The resulting system was energy minimized, initially by fixing the backbone atoms, and later releasing the constraints on them. All the atoms were then propagated according to Newton's equations of motions using the leapfrog Verlet integrator with a time step of 2 fs. The solvated protein was equilibrated for 100 ps, and the structure at the end of equilibration was used to start the simulations of the protein bound to larger ions by replacing Mg^{2+} with Ca^{2+}, Sr^{2+}, or Ba^{2+}. The resulting structures were first energy minimized to relieve any bad contacts and equilibrated further for another 10 ps. Each metal−protein complex was subjected to 100 ps of production dynamics, and the resulting binding site will be referred to as "site" 1 (see also Results).

Simulations were also carried out starting from the hydrogen-built X-ray structure of the Mg^{2+}-bound protein with Mg^{2+} displaced roughly 2 Å toward D70 (Figure 1) so that it could interact with the D70 side chain. The resulting structure was energy minimized, solvated, and equilibrated for 100 ps, and the structure at the end of equilibration was used as the starting point for the simulations of the protein bound to Ca^{2+}, Sr^{2+}, or Ba^{2+}, as described above. Each of the equilibrated metal−protein complexes was subjected to 100 ps of production dynamics, and the resulting binding environment will be referred to as "site" 2 (see also Results). The term "site" is used here for brevity even though "site" 2 does not involve a totally new location, but rather a different environment of the metal. The final structure for RNase H1 with Ca^{2+} bound in either "site" 1 or "site" 2 was used to set up the free energy calculations as the free energies were obtained relative to that of Ca^{2+} (see below).

IV. Analyses. Average ion−ligand distances, ion−solvent radial distribution functions, and the average electrostatic potential at the ion due to protein and solvent molecules were computed from the 100 ps trajectories of RNase H1 with metal ions bound in the two binding sites. Since an amino acid residue is more polarizable than a water molecule, it is expected to donate more charge to a given metal, thus forming stronger interactions with the metal (shorter metal−O distance) compared with a water molecule. Therefore, for a given metal in a protein, amino acid ligands whose ion−O distances are ≤ the respective ion−O(water) distance were considered to belong to the first shell of the metal. The ensemble averaged ion−ligand distances were used in the constrained binding free energy computations (see below).

V. Relative Binding Free Energies. These were computed using the thermodynamic cycle shown in Scheme 1:[40]

$$\Delta\Delta G^{bind} = \Delta G^{M} - \Delta G^{Ca} = \Delta\Delta G_{solv}^{prot} - \Delta\Delta G_{solv}^{aq} \quad (1)$$

where M = Mg^{2+}, Sr^{2+}, or Ba^{2+}, and $\Delta\Delta G_{solv}^{aq}$ and $\Delta\Delta G_{solv}^{prot}$ are the average free energies for converting Ca^{2+} to M in aqueous solution and in the protein, respectively. All the free energies were evaluated relative to Ca^{2+} to effectively minimize the errors stemming from the truncation of the long-range Coulombic energies.

(34) Brooks, B. R.; Bruccoleri, R. E.; Olafson, B. D.; States, D. J.; Swaminathan, S.; Karplus, M. *J. Comput. Chem.* **1983**, *4*, 187.
(35) Jorgensen, W. L.; Chandrasekhar, J.; Madura, J. D.; Impey, R. W.; Klein, M. L. *J. Chem. Phys.* **1983**, *79*, 926.
(36) MacKerell, J. A. D.; Bashford, D.; Bellott, M.; Dunbrack, R.; Evanseck, J. D.; Field, M. J.; Fischer, S.; Gao, J.; Guo, H.; Ha, S.; Joseph-McCarthy, D.; Kuchnir, L.; Kuczera, K.; Lau, F. T. K.; Mattos, C.; Michnick, S.; Ngo, T.; Nguyen, D. T.; Prodhom, B.; Reiher, W. E. I.; Roux, B.; Schlenkrich, M.; Smith, J. C.; Stote, R.; Straub, J.; Watanabe, M.; Wiorkiewicz-Kuczera, J.; Yin, D.; Karplus, M. *J. Phys. Chem. B* **1998**, *102*, 3586.
(37) Åqvist, J. *J. Phys. Chem.* **1990**, *94*, 8021.

(38) Ryckaert, J. P.; Ciccotti, G.; Berendsen, H. J. C. *J. Comput. Phys.* **1977**, *23*, 327.
(39) Mezei, M. *J. Comput. Chem.* **1997**, *18*, 812.
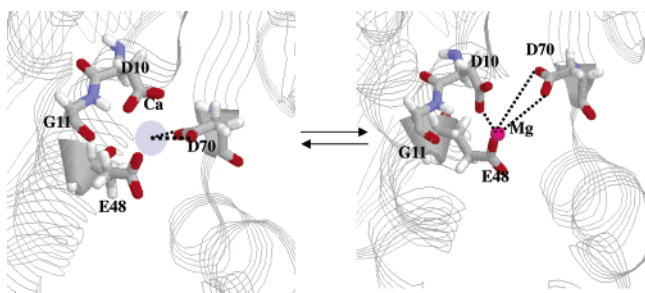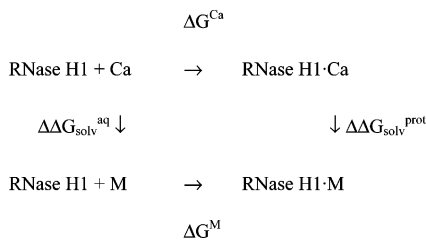(40) Tembe, B. L.; McCammon, J. A. *Comput. Chem.* **1984**, *8*, 281.

Figure 2. A schematic diagram for the interconversion between Mg^{2+} bound at the X-ray binding site and Ca^{2+} at a cavity site formed by the three acidic residues, D10, E48, and D70. The dashed lines represent the fictitious forces applied for the reactant and product states (see Methods).

Scheme 1

$$\Delta G^{Ca}$$

RNase H1 + Ca $\rightarrow$ RNase H1·Ca

$\Delta\Delta G_{solv}^{aq} \downarrow$ $\downarrow \Delta\Delta G_{solv}^{prot}$

RNase H1 + M $\rightarrow$ RNase H1·M

$$\Delta G^{M}$$

Relative binding free energies, $\Delta\Delta G^{bind}$, for Mg^{2+}, Sr^{2+}, and Ba^{2+} were computed assuming that the metal dication and Ca^{2+} are bound in the same site, that is, either "site" 1 or "site" 2. Relative binding free energy, $\Delta\Delta G^{bind}$, for Mg^{2+} was also computed assuming that Mg^{2+} binds at "site" 1, while Ca^{2+} binds at "site" 2. Such free energy calculations required applying fictitious forces, as shown by the dotted lines in Figure 2, to pull the ion from "site" 1 to "site" 2 and vice versa. In converting Ca^{2+} in "site" 2 to Mg^{2+} in "site" 1, $\lambda = 0$ corresponds to Ca^{2+} artificially bonded to the D70 carboxylate oxygen atoms in a bidentate mode with equilibrium bond distances set at the average ion−oxygen distances obtained from the simulation of Ca^{2+} in "site" 2 (Figure 2). On the other hand, $\lambda = 1$ corresponds to Mg^{2+} artificially bonded to D10 and D70 with bond distances set at the average ion−oxygen distances of the respective carboxylate groups obtained from the simulations of Mg^{2+} in "site" 1 (Figure 2). A weak force constant of 10 kcal/mol·Å was used for all the fictitious bonds in Figure 2.

The energies from the fictitious forces were not taken into account in computing the free energies using thermodynamic integration. However, this does not completely eliminate the effect of the fictitious forces. Thus, the free energy obtained should be treated as indicative of qualitative trends, providing possible binding modes for Mg^{2+} and Ca^{2+}. The free energy trend obtained from thermodynamic integration was subsequently verified using a combined DFT/CDM approach (see below).

The free energy simulations were carried out using the same protocol as described above. They were based on a thermodynamic integration approach with $\lambda = 0$ corresponding to Ca^{2+} and $\lambda = 1$ corresponding to M in the forward direction, and vice versa in the reverse direction.[41] The integration protocol employed 16 window points at $\lambda = 0.01, 0.03, 0.05, 0.1, 0.2, 0.3, 0.4, 0.5, 0.6, 0.7, 0.8, 0.9, 0.92, 0.95, 0.97,$ and 0.99. The windows were chosen to adequately sample the steeply varying parts of the energy derivatives. The free energies at the endpoints ($\lambda = 0$ and $\lambda = 1$) were obtained using a free energy perturbation approach employing a double-wide sampling scheme to avoid divergence at the endpoints.[41] At each window point, the system was equilibrated for 10 ps followed by 20 ps of production dynamics. Perturbation energies were collected every 4 fs for computing the

relative free energies. The reverse perturbations were performed from a configuration that is independent from the forward perturbation runs. The free energies for the forward and reverse runs were then averaged.

DFT/CDM Calculations. I. Models Used in DFT Calculations. Formate ($HCOO^-$) was used as a model for deprotonated Asp and Glu side chains, while formamide ($HCONH_2$) was employed as a model for the backbone peptide group. Since Mg^{2+} complexes in water and proteins are predominantly octahedral,[4,42−44] we considered clusters of the type $[Mg(H_2O)_{6-i}L_i]$, where L is an inner-shell $HCOO^-$ or $HCONH_2$ ligand and $i = 0,...,3$. Thus, the X-ray metal-binding site, in which Mg^{2+} is bound to the D10 and E48 side chains as well as the G11 backbone (Figure 1a), was modeled as $[Mg(H_2O)_3(HCOO^-)_2HCONH_2]^0$.

Ca^{2+} exhibits a wide variation in the number of first-shell water molecules. Experimental (X-ray and neutron diffraction) and theoretical studies on Ca^{2+} water solutions yield a coordination number ranging between 6 and 10 with 7 or 8 appearing to be the most common.[43,45] Therefore, both heptacoordinated $[Ca(H_2O)_7]^{2+}$ and octacoordinated $[Ca(H_2O)_8]^{2+}$ aqua complexes were considered. In proteins, however, Ca^{2+} seems to prefer heptacoordination,[4] so only 7-coordinated Ca^{2+} protein complexes were modeled. As Ca^{2+} is found to bind monodentately and bidentately to carboxylates in the X-ray structures, both carboxylate binding modes were considered.

II. Exchange Free Energies in the Gas Phase. The DFT calculations employed Becke's three-parameter hybrid method[46] in conjunction with the Lee, Yang, and Parr correlation functional[47] and the 6-31++G-(2d,2p) basis set. In previous studies, we had calibrated the B3LYP/6-31++G(2d,2p) calculations with respect to available experimental data and showed that they are well suited for evaluating the geometries and free energies of interaction of complexes between divalent cations and oxygen-/nitrogen-containing ligands.[33,48] Consequently, *full geometry optimization* for each metal complex was carried out at the B3LYP/6-31++G(2d,2p) level using the Gaussian 98 program.[49] Vibrational frequencies were then computed at the same level of theory/basis to verify that each complex was at the minimum of its potential energy surface. *No imaginary frequency was found in any of the complexes.* After scaling the frequencies by an empirical factor of 0.9613,[50] we evaluated the zero-point energy (ZPE), thermal energy (E_T), work (PV), and entropy (S) corrections using standard statistical mechanical formulas.[51] The differences ΔE_{elec}, ΔZPE, ΔE_T, ΔPV, and ΔS between the products and reactants were employed to compute the reaction free energy at room temperature, $T = 298.15$ K, according to the following expression:
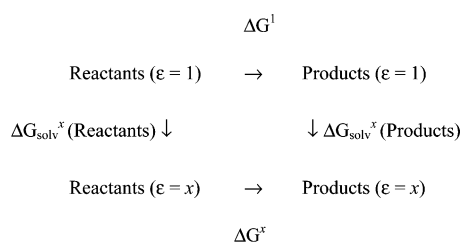
$$\Delta G^1 = \Delta E_{elec} + \Delta ZPE + \Delta E_T + \Delta PV - T\Delta S \qquad (2)$$

III. Exchange Free Energies in the Protein. The reaction free energy in a given environment characterized by a dielectric constant ϵ

(41) Beveridge, D. L.; DiCapua, F. M. *Annu. Rev. Biophys. Biophys. Chem.* **1989**, *18*, 439.

(42) Cotton, F. A.; Wilkinson, G. *Advanced Inorganic Chemistry* John Wiley & Sons: New York, 1980.

(43) Marcus, Y. *Chem. Rev.* **1988**, *88*, 1475.

(44) Bock, C. W.; Katz, A. K.; Markham, G. D.; Glusker, J. P. *J. Am. Chem. Soc.* **1999**, *121*, 7360.

(45) Katz, A. K.; Glusker, J. P.; Beebe, S. A.; Bock, C. W. *J. Am. Chem. Soc.* **1996**, *118*, 5752.

(46) Becke, A. D. *J. Chem. Phys.* **1993**, *98*, 5648.

(47) Lee, C.; Yang, W.; Parr, R. G. *Phys. Rev.* **1988**, *B37*, 785.

(48) Dudev, T.; Lim, C. *J. Phys. Chem. B* **2001**, *105*, 10709.

(49) Frisch, M. J.; Trucks, G. W.; Schlegel, H. B.; Scuseria, G. E.; Robb, M. A.; Cheeseman, J. R.; Zakrzewski, V. G.; Montgomery, J. A., Jr.; Stratmann, R. E.; Burant, J. C.; Dapprich, S.; Millam, J. M.; Daniels, A. D.; Kudin, M.; Strain, K. N.; Farkas, O.; Tomasi, J.; Barone, V.; Cossi, M.; Cammi, R.; Mennucci, B.; Pomelli, C.; Adamo, C.; Clifford, S.; Ochterski, J.; Petersson, G. A.; Ayala, P. Y.; Cui, Q.; Morokuma, K.; Malick, D. K.; Rabuck, A. D.; Raghavachari, K.; Foresman, J. B.; Cioslowski, J.; Ortiz, J. V.; Stefanov, B. B.; Liu, G.; Liashenko, A.; Piskorz, P.; Komaromi, I.; Gomperts, R.; Martin, R. L.; Fox, D. J.; Keith, T.; Al-Laham, M. A.; Peng, C. Y.; Nanayakkara, A.; Gonzalez, C.; Challacombe, M.; Gill, P. M. W.; Johnson, B.; Chen, W.; Wong, M. W.; Andres, J. L.; Gonzalez, C.; Head-Gordon, M.; Replogle, E. S.; Pople, J. A. *Gaussian 98*, revision A.5; Gaussian, Inc.: Pittsburgh, PA, 1998.

(50) Wong, M. W. *Chem. Phys. Lett.* **1996**, *256*, 391.

(51) McQuarrie, D. A. *Statistical Mechanics*; Harper and Row: New York, 1976.

Scheme 2

$$\Delta G^1$$

Reactants ($\varepsilon = 1$) $\rightarrow$ Products ($\varepsilon = 1$)

ΔG_{solv}^x(Reactants) $\downarrow$ $\qquad$ $\downarrow \Delta G_{solv}^x$(Products)

Reactants ($\varepsilon = x$) $\rightarrow$ Products ($\varepsilon = x$)

$$\Delta G^x$$

$= x$ can be calculated according to the thermodynamic cycle shown in Scheme 2. ΔG^1 is the gas-phase free energy computed using eq 2. ΔG_{solv}^x is the free energy for transferring a molecule in the gas phase to a continuous solvent medium characterized by a dielectric constant, x. By solving Poisson's equation using finite difference methods[52,53] to estimate ΔG_{solv}^x (see below), the reaction free energy in an environment modeled by dielectric constant x, ΔG^x, can be computed from

$$\Delta G^x = \Delta G^1 + \Delta G_{solv}^x(\text{products}) - \Delta G_{solv}^x(\text{reactants}) \quad (3)$$

The continuum dielectric calculations employed a $71 \times 71 \times 71$ lattice with an initial grid spacing of 1.0 Å, refined with a spacing of 0.25 Å, ab initio geometries, and natural bond orbital (NBO) atomic charges.[54] The low-dielectric region of the solute was defined as the region inaccessible to contact by a 1.4 Å radius sphere rolling over the molecular surface. This region was assigned a dielectric constant of two ($\epsilon_{in} = 2$) to account for the electronic polarizability of the solute. The molecular surface was defined by effective solute radii, which were obtained by adjusting the CHARMM22[36] van der Waals radii to reproduce the experimental hydration free energies of the metal cations and ligands. These radii had been optimized in our previous studies[33,48,55,56] and are as follows (in Å): $R_{Mg} = 1.50$, $R_{Ca} = 1.75$, $R_O(\text{HCOO}^-) = 1.65$, $R_O(\text{H}_2\text{O}) = 1.69$, $R_O(\text{HCONH}_2) = 1.79$, $R_N = 1.70$, $R_C = 1.90$, $R_H(\text{H}_2\text{O}) = 1.0$, $R_H(\text{C, N}) = 1.468$. Buried metal-binding sites were characterized with an external dielectric constant ϵ_{out} equal to 2, while partially buried sites were assigned ϵ_{out} equal to 4 or 10 depending on their relative solvent accessibility.[52,57] Thus, Poisson's equation was solved with ϵ_{out} equal to 1, 2, 4, or 10 and $\epsilon_{in} = 2$. The difference between the computed electrostatic potentials in a given dielectric medium ($\epsilon = x$) and in the gas phase ($\epsilon = 1$) yielded the solvation free energy ΔG_{solv}^x of the metal complex.

Results

MD Simulation Results. I. Force Field Calibration. First, the accuracy of the force field parameters listed in Table 1 was assessed by computing structural and thermodynamic properties of Mg^{2+}, Ca^{2+}, Sr^{2+}, and Ba^{2+} from MD simulations of these ions in water. The results in Table 2 show that the ion−O(water) distance of the first-shell water molecules and the respective coordination number are in accord with experimental data from various sources such as neutron diffraction, EXAF, and X-ray diffraction.[43,58] In addition to the solvation structure, the hydration free energies for these ions relative to Ca^{2+} are also in close agreement with the experimental numbers (see Table 2).[59] The computed relative solvation free energies, $\Delta\Delta G_{solv}^{aq}$, were used in computing the free energies of metal ions binding to the protein (see eq 1 and below).

(52) Gilson, M. K.; Honig, B. *Biopolymers* **1986**, *25*, 2097.
(53) Lim, C.; Bashford, D.; Karplus, M. *J. Phys. Chem.* **1991**, *95*, 5610.
(54) Reed, A. E.; Curtiss, L. A.; Weinhold, F. *Chem. Rev.* **1988**, *88*, 899.
(55) Dudev, T.; Lim, C. *J. Phys. Chem. B* **2000**, *104*, 3692.
(56) Dudev, T.; Lim, C. *J. Am. Chem. Soc* **2002**, *124*, 6759.
(57) Harvey, S. C.; Hoekstra, P. *J. Phys. Chem.* **1972**, *76*, 2987.
(58) Marcus, Y. *J. Chem. Soc., Faraday Trans.* **1991**, *87*, 2995.
(59) Friedman, H. L.; Krishnan, C. V. *Thermodynamics of ionic hydration*; Plenum Press: New York, 1973; Vol. 3.

Table 2. Computed and Experimental Structural and Thermodynamics Properties of Alkaline Earth Metal Dications in Water

ion	R_{ion}^a (Å)	R_{Born}^b (Å)	R_{ion-O}^c (Å)	CN^d	$\Delta\Delta G_{solv}^e$ (kcal/mol)	$\Delta G_{solv}(\text{expt})^f$ (kcal/mol)
Mg^{2+}	0.78 (0.72)	1.44	2.03 ± 0.06 (2.09)	6 (6)	-75.62 ± 0.11 (-74)	-455.5
Ca^{2+}	1.06 (1.00)	1.72	2.45 ± 0.10 (2.42)	7.5 (7−8)	0.0	-380.8
Sr^{2+}	1.27 (1.25)	1.90	2.65 ± 0.11 (2.64)	8.5 (8)	32.97 ± 0.36 (34)	-345.9
Ba^{2+}	1.43 (1.36)	2.08	2.82 ± 0.08 (2.90)	9 (9.5)	63.10 ± 1.75 (65)	-315.1

^{a} Goldschmidt ionic radii from Cotton and Wilkinson[42] and Pauling ionic radii (in brackets) from Marcus.[43] ^{b} Born radius computed from experimental free energies in the last column; i.e., $R_{Born} = 655.5/\Delta G_{solv}$. ^{c} Average ion−oxygen distances computed from simulations in this work using the parameters in Table 1; experimental values taken from Marcus[43,58] are in parentheses. ^{d} The computed ion−water coordination numbers in the first solvation shell; experimental values taken from Marcus[43,58] are in parentheses. ^{e} The computed and experimental (in parentheses) hydration free energies relative to the hydration free energy of Ca^{2+}. ^{f} Experimental hydration free energies from Friedman & Krishnan.[59]
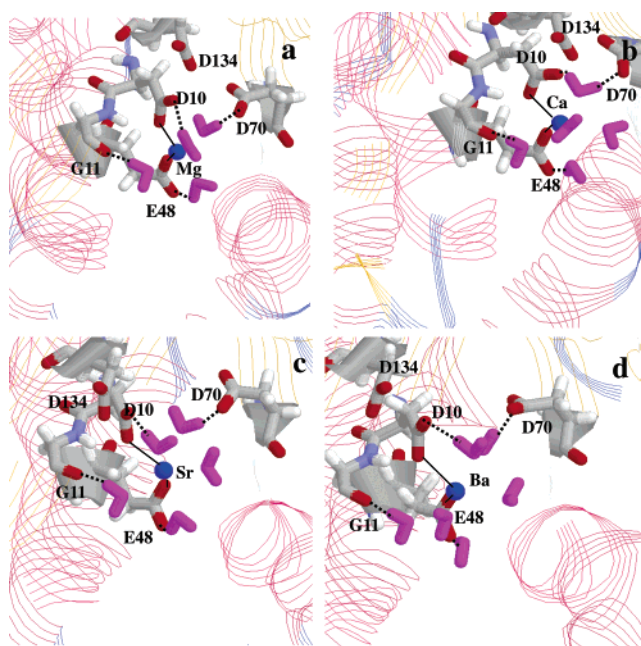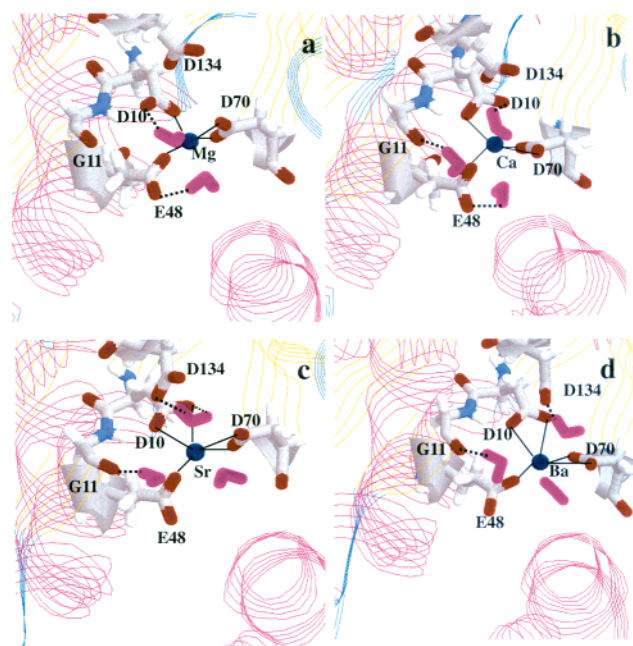

Figure 3. Average MD structure of Mg^{2+} (a), Ca^{2+} (b), Sr^{2+} (c), and Ba^{2+} (d) at binding "site" 1. The metal ions are in blue, the bound water molecules are in magenta, and hydrogen bonds involving the metal ligands are indicated by the dotted lines. For the sake of clarity, only the metal−protein ligand (but not the metal-bound water) interactions are shown as solid lines.

II. "Site" 1 Conformations. In the X-ray structure (PDB entry 1RDD), Mg^{2+} is within 2.5 Å of the carbonyl oxygen of G11 and one of the carboxylate oxygen atoms of D10 and E48, while it is greater than 4.2 Å and 5.3 Å from the D70 and D134 side chain oxygen atoms, respectively (see Figure 1); no water molecules were seen due to the low (2.8 Å) resolution of this structure. Starting from this X-ray structure the simulation of Mg^{2+}-bound RNase H1 (Figure 3a) shows that Mg^{2+} is still within 2 Å of one of the carboxylate oxygen atoms of D10 and E48, but it is 4.3 ± 0.1 Å from the weakly bound carbonyl oxygen of G11. The simulations of the protein bound to the larger dications (Ca^{2+}, Sr^{2+}, and Ba^{2+} in Figure 3b−d, respectively) also show that, in each case, the metal is bound by two acidic side chains; such an environment will be referred to as "site" 1 (see also Methods). In this binding site, Mg^{2+} is

Figure 4. Average MD structure of Mg^{2+} (a), Ca^{2+} (b), Sr^{2+} (c), and Ba^{2+} (d) at binding "site" 2. The metal ions are in blue, the bound water molecules are in magenta, and hydrogen bonds involving the metal ligands are indicated by the dotted lines. For the sake of clarity, only the metal−protein ligand (but not the metal-bound water) interactions are shown as solid lines.

octahedrally coordinated to the D10 and E48 carboxylate oxygen atoms in a monodentate fashion and four water molecules (Figure 3a). Ca^{2+}, Ba^{2+}, and Sr^{2+} differ from Mg^{2+} in binding to one or two more water molecules so that the coordination number is seven for Ca^{2+}, between seven and eight for Sr^{2+}, and eight for Ba^{2+}. The nearby D70 side chain is more than 4.5 Å from each ion, as in the X-ray structure, but it forms hydrogen bonds with the metal-bound water molecules in all the simulations. In addition to D70, the metal-free carboxylate oxygen atoms of D10 and E48 as well as the carbonyl oxygen of G11 also form hydrogen bonds with the metal-bound water molecules in all the simulations. The network of protein−water hydrogen bonds presumably stabilizes the metal complex.

III. "Site" 2 Conformations. To explore the possibility that the metal dication could bind to D70 and thus inhibit enzymatic activity (see Introduction), simulations were also carried out with the metal bound to D70. The resulting average structures of the metal-binding sites in Figure 4a−d show that in each case, the metal is bound by three acidic side chains; such a site will be referred to as "site" 2. In this site, Mg^{2+} and Ca^{2+} are coordinated monodentately to D10 and E48 but bidentately to D70 (Figures 4a and 4b), while Sr^{2+} and Ba^{2+} differ from the smaller ions by forming bidentate (as opposed to monodentate) bonds with D10 (Figures 4c and 4d). The increase in the number of metal−amino acid interactions in "site" 2 relative to "site" 1 is offset by a corresponding decrease in the number of metal−water interactions so that the coordination numbers of the metal ions are the same as those found in "site" 1. As for "site" 1, the metal complex is stabilized by hydrogen bonds between the metal-free carboxylate oxygen atoms and the metal-bound water molecules. The carbonyl oxygen of G11 forms strong hydrogen bonds with a water molecule bound to Ca^{2+}, Sr^{2+}, or Ba^{2+}. However, such an interaction is absent in the Mg^{2+}-binding site (see Figure 4a).
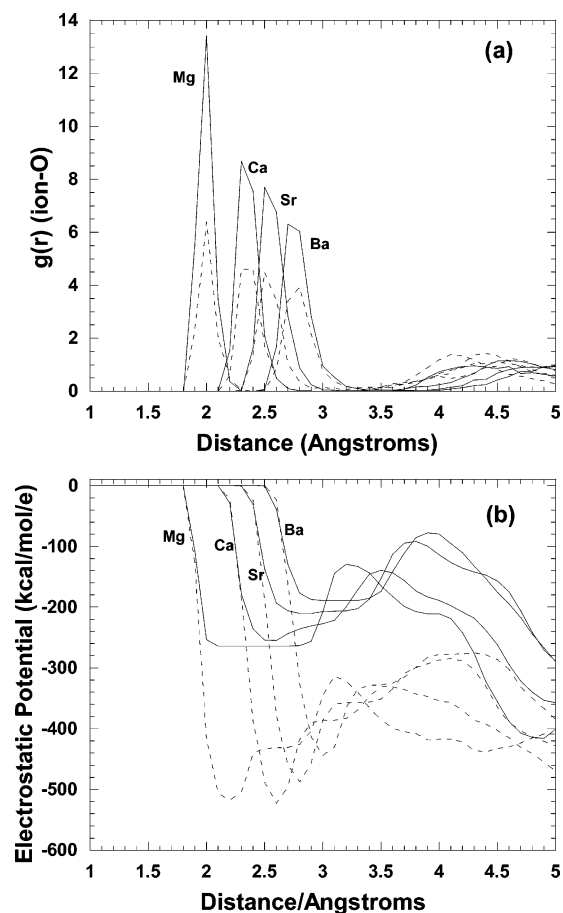

Figure 5. Ion−O(water) radial distribution function (a) and electrostatic potential at the ion due to the protein (b) in binding "site" 1 (solid curves) and "site" 2 (dashed curves).

IV. Differences between "Site" 1 and "Site" 2. The key difference between the two sites is that, in "site" 2, the metal binds bidentately to both D70 carboxylate oxygen atoms at the expense of water molecules. The decrease in the metal−water interactions in "site" 2 compared to "site" 1 is illustrated in Figure 5a, which shows the ion−O(water) distribution functions around the ions for "site" 1 (solid curves) and "site" 2 (dashed curves). Clearly, the peak heights of the dashed curves are significantly smaller than those of the solid curves, showing that fewer water molecules are in "site" 2 compared to "site" 1. On average, Mg^{2+}, Ca^{2+}, Sr^{2+}, and Ba^{2+} are coordinated respectively to 2, 3, 2−3, and 3 water molecules in "site" 2 but to 4, 5, 5−6, and 6 water molecules in "site" 1.

The corresponding increase in the metal−protein interactions in "site" 2 compared to "site" 1 is evident from Figure 5b, which shows the potential contributions from only the protein atoms to the electrostatic potential at the center of the ion as a function of distance from the ion. The absolute electrostatic potentials from the *first-shell* ligands in "site" 1 (Figure 5b, solid curves) are more positive than those in "site" 2 (Figure 5b, dashed curves) due to fewer metal−protein interactions in the former compared to the latter (see above). Another difference is that they exhibit flatter wells than those in "site" 2, reflecting the monodentate and bidentate binding of acidic groups in "site" 1 and "site" 2, respectively. Interestingly, the potential well depths for Mg^{2+} and Ca^{2+} in "site" 2 are similar, whereas the potential
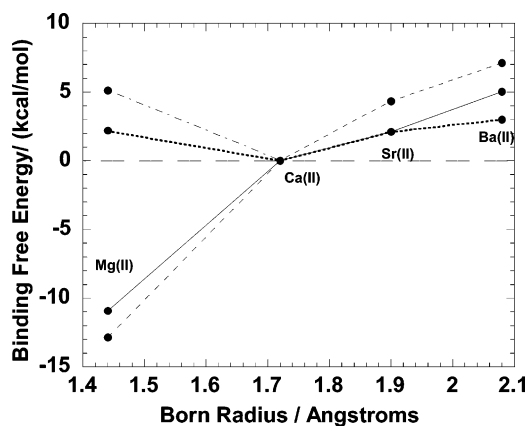
Figure 6. Computed and experimental binding free energies as a function of the Born radius. The solid, dashed, and dotted curves are data based on "site" 1, "site" 2, and experiment, respectively. The dash−dot curves are data based on Mg^{2+} binding in "site" 1 and Ca^{2+} in "site" 2.

Table 3. Experimental Free Energies (ΔG), Enthalpies (ΔH), and Entropies (ΔS) for Alkaline Earth Metal Dication Binding to RNase H1 in Aqueous Solution

cofactor	K (M^{-1})	ΔG (kcal/mol)	ΔH (kcal/mol)	ΔS (cal/mol/K)
Mg^{2+}	$1.1(\pm0.2) \times 10^4$	-5.5 ± 0.1	-2.6 ± 0.1	9.7 ± 0.7
Ca^{2+}	$4.4(\pm1.2) \times 10^5$	-7.7 ± 0.1	-10.8 ± 0.2	-10.4 ± 0.6
Sr^{2+}	$6.5(\pm0.3) \times 10^3$	-5.2 ± 0.1	-3.2 ± 0.3	6.7 ± 1.1
Ba^{2+}	$2.8(\pm0.2) \times 10^3$	-4.7 ± 0.1	-1.4 ± 0.2	11.1 ± 0.8

well depth for Mg^{2+} in "site" 1 is more negative than that of Ca^{2+} in the same site.

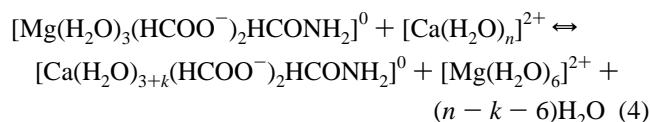**V. Relative Binding Free Energies in "Site" 1 or "Site" 2.** As the structures in sites 1 and 2 were very stable during the course of the simulations, both sites were used to compute the metal binding free energies relative to the Ca^{2+} binding free energy. The metal binding free energies are plotted as a function of Born radii, R_{Born}, derived from experimental hydration free energies (Table 2), in Figure 6 for "site" 1 (solid curve) and "site" 2 (dashed curve). For both sites 1 and 2, Mg^{2+}, Ca^{2+}, Sr^{2+}, and Ba^{2+} bind successively weaker to the protein. Although the metal-binding free energy becomes less favorable (more positive) with increasing Born radius, the relationship between the free energy and the Born radius is not linear, as in the case of metal binding in aqueous solution where ΔG_{solv} exhibits a linear function of $1/R_{Born}$.[60,61] This indicates that the protein environment plays a significant role in guiding the metal binding.

VI. Comparison between Experimental and Computed Relative Binding Free Energies. Comparison of the computed binding free energies (Figure 6, solid and dashed curves) with the corresponding experimental data (Figure 6, dotted curve) shows that if the alkaline earth metals bind in the same site (1 or 2) the absolute binding free energy for Mg^{2+} is severely overestimated: Mg^{2+} is predicted to bind the protein more tightly than Ca^{2+}, in contrast to the experimental findings (Table 3). However, the bigger Sr^{2+} and Ba^{2+} ions are predicted to bind the protein less tightly than Ca^{2+}, in accord with experimental findings. In fact, the computed relative binding free energies of Sr^{2+} and Ba^{2+} in "site" 1 are close to the respective experimental values.

(60) Born, M. Z. *Phys.* **1920**, *1*, 45.
(61) Babu, C. S.; Lim, C. *J. Phys. Chem. B* **1999**, *103*, 7958.

A clue to the observed discrepancy between the computed and measured binding free energy of Mg^{2+} relative to Ca^{2+} stems from both experimental and theoretical findings. Ca^{2+} has the most negative binding enthalpy (-10.8 kcal/mol) compared with the other metal ions (see Table 3). This experimental finding correlates with the observation that the potential well depth for Ca^{2+} in "site" 2 is much deeper than that for the other dications in "site" 1 (see Figure 5b) due presumably to the additional interactions between Ca^{2+} and bidentate D70 in "site" 2, which are absent in "site" 1. These observations suggest that Ca^{2+} binds at "site" 2, while Mg^{2+} binds at "site" 1 (see Figure 7). To verify this hypothesis, the free energy for Mg^{2+} binding in "site" 1 relative to Ca^{2+} in "site" 2 was computed by applying fictitious forces, as shown in Figure 2 (see Methods). The predicted free energy of Mg^{2+} relative to Ca^{2+} (Figure 6, dash-dotted curve) is in qualitative agreement with the experimental trend (Figure 6, dotted curve) in that Ca^{2+} binds more tightly than Mg^{2+} to RNase H1.

DFT/CDM Results. To verify that Ca^{2+} binds at "site" 2, while the native cofactor, Mg^{2+}, binds at the X-ray binding site, we also computed the free energy of $Mg^{2+}\leftrightarrow Ca^{2+}$ exchange in model binding sites of RNase H1 using combined DFT/CDM calculations, as described in Methods.

I. Metal Ion Exchange in the X-ray Binding Site Assuming No Conformational Change. We first considered metal exchange in the X-ray metal-binding site, which was modeled as $[Mg(H_2O)_3(HCOO^-)_2HCONH_2]^0$ (Figure 8a), and assumed no change in the protein ligand surrounding of the metal ion upon exchange; that is,

$$[Mg(H_2O)_3(HCOO^-)_2HCONH_2]^0 + [Ca(H_2O)_n]^{2+} \leftrightarrow$$
$$[Ca(H_2O)_{3+k}(HCOO^-)_2HCONH_2]^0 + [Mg(H_2O)_6]^{2+} +$$
$$(n - k - 6)H_2O \quad (4)$$

In eq 4, $n = 7$ or 8, and $k = 0$, 1; the exchange free energies are given in Table 4. In replacing Mg^{2+} with Ca^{2+}, four different exchange reactions were modeled because in aqueous solution Ca^{2+} can be heptacoordinated ($n = 7$ in eq 4, first two reactions in Table 4) or octacoordinated ($n = 8$ in eq 4, last two reactions in Table 4). Ca^{2+} can also bind a carboxylate group monodentately (Figure 8b, reactions 1 and 3 in Table 4) or bidentately (Figure 8c, reactions 2 and 4 in Table 4).

The gas-phase enthalpies and free energies for the four $Mg^{2+} \rightarrow Ca^{2+}$ reactions are positive, ranging from 20−42 and 24−28 kcal/mol, respectively. The entropy for the first $Mg^{2+} \rightarrow Ca^{2+}$ reaction is negative ($T\Delta S = -5.0$ kcal/mol), whereas the $T\Delta S$ values for the other three $Mg^{2+} \rightarrow Ca^{2+}$ reactions are positive due to the release of one or two water molecules. In a buried or relatively solvent exposed cavity, ΔG^x ($x = 2-10$) are all positive, except ΔG^{10} for the last reaction, whose small negative value is within the error limits (± 2 kcal/mol) of the calculations. This implies that exchanging Mg^{2+} for Ca^{2+} in the X-ray metal-binding site, without changing the protein ligand surrounding, is thermodynamically unfavorable regardless of the carboxylate-binding mode to the metal. In other words, Mg^{2+} is predicted to have a higher affinity for the X-ray metal-binding site than Ca^{2+}, in accord with the simulation results (Figure 6, solid curve) but in contrast to the experimental findings.

II. Metal Ion Exchange Accompanied by a Conformational Change. The MD simulations suggest that, upon substi-
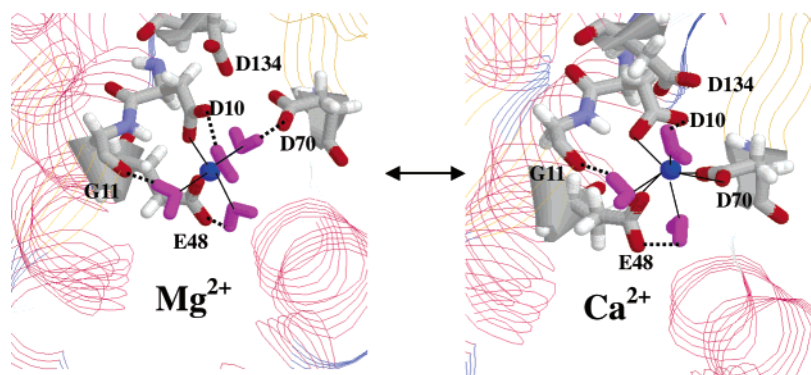
Figure 7. Preferred binding environment of Mg^{2+} ("site" 1) and Ca^{2+} ("site" 2). The bound water molecules are in magenta.
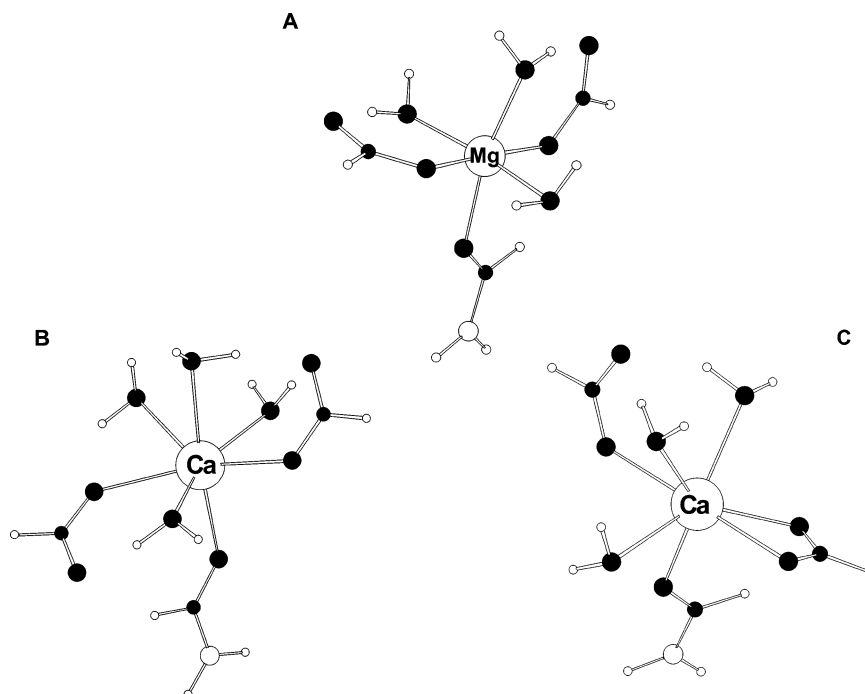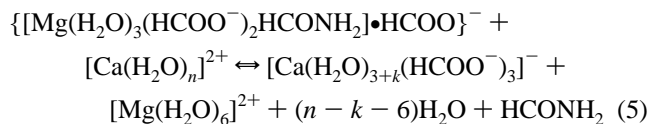

Figure 8. Fully optimized B3LYP/6-31++G(2d,2p) structures of the model X-ray Mg^{2+}-binding site, $[Mg\ W_3\ (HCOO^-)_2\ HCONH_2]^0$ (a), the Mg^{2+}-binding site with Mg^{2+} replaced by Ca^{2+} binding monodentately to both carboxylates (b) or binding monodentately to one carboxylate and bidentately to the other (c).

Table 4. Enthalpies (ΔH^1) and Free Energies (ΔG^x) (in kcal/mol) of Exchanging Mg^{2+} for Ca^{2+} in the X-ray Binding Site Characterized by Dielectric Constant x

reaction[a]	$\Delta H^{1,b}$	ΔG^1	ΔG^2	ΔG^4	ΔG^{10}
$[MgW_3(HCOO^-)_2HCONH_2]^0 + [CaW_7]^{2+} \rightarrow [CaW_4(HCOO^-)_2HCONH_2]^0 + [MgW_6]^{2+}$	20.2	25.2	17.2	13.7	11.7
$[MgW_3(HCOO^-)_2HCONH_2]^0 + [CaW_7]^{2+} \rightarrow [CaW_3(HCOO^-)(HC\tilde{O}\tilde{O}^-)HCONH_2]^0 + [MgW_6]^{2+} + W$	30.0	24.0	13.3	7.5	3.5
$[MgW_3(HCOO^-)_2HCONH_2]^0 + [CaW_8]^{2+} \rightarrow [CaW_4(HCOO^-)_2HCONH_2]^0 + [MgW_6]^{2+} + W$	32.2	28.2	16.5	10.8	7.3
$[MgW_3(HCOO^-)_2HCONH_2]^0 + [CaW_8]^{2+} \rightarrow [CaW_3(HCOO^-)(HC\tilde{O}\tilde{O}^-)HCONH_2]^0 + [MgW_6]^{2+} + 2W$	41.9	27.0	12.6	4.6	−0.9

[a] W denotes H_2O; $HC\tilde{O}\tilde{O}^-$ indicates that both carboxylate oxygen atoms interact with the metal ion, whereas $HCOO^-$ denotes that only one of the carboxylate oxygen atoms interacts with the metal ion. [b] Calculated at the B3LYP/6-31++G(2d,2p) level.

tuting Mg^{2+}, Ca^{2+} can bind in a different environment consisting of three carboxylates (D70, D10, E48) and three water molecules ("site" 2). In the X-ray metal-binding site, the second-shell D70 appears to be hydrogen bonded to first-shell water molecules; thus, the X-ray metal-binding site including D70 was modeled as shown in Figure 9a. $Mg^{2+} \rightarrow Ca^{2+}$ exchange was modeled as

$$\{[Mg(H_2O)_3(HCOO^-)_2HCONH_2] \bullet HCOO\}^- +$$
$$[Ca(H_2O)_n]^{2+} \leftrightarrow [Ca(H_2O)_{3+k}(HCOO^-)_3]^- +$$
$$[Mg(H_2O)_6]^{2+} + (n-k-6)H_2O + HCONH_2 \quad (5)$$

In eq 5, $n = 7$ or 8; $k = 0$ or 1; and $\bullet$ denotes inner/outer-shell interactions in the X-ray Mg^{2+}-binding site (Figure 9a).

All the reactions in Table 5 have positive entropies due to the release of one or two water molecules and/or formamide. The free energies follow the same trends of changes observed for eq 4 (Table 4), becoming less positive with increasing ϵ. In particular, the ΔG^4 and/or ΔG^{10} for the last three reactions in Table 5 become negative. The $Mg^{2+} \rightarrow Ca^{2+}$ exchange depends on the mode of carboxylate binding to Ca^{2+} and the solvent accessibility of the metal-binding site. If Ca^{2+} is bound monodentately to all three acidic residues (Figure 9b) in a
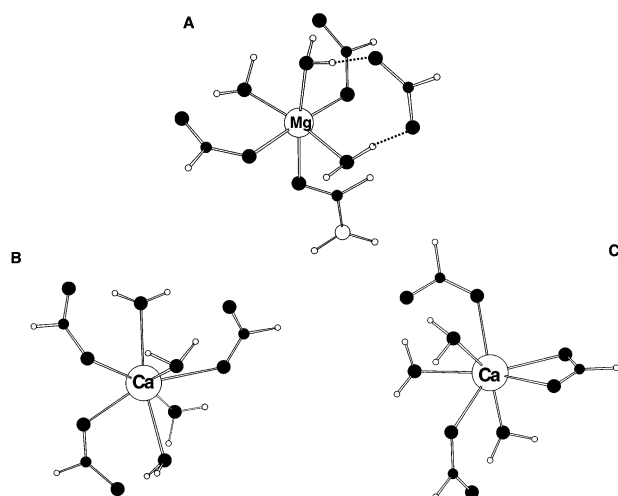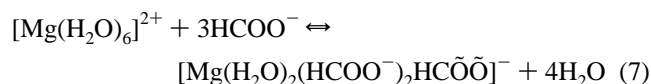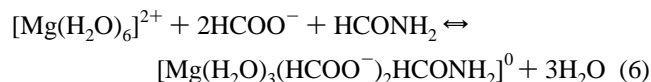
Figure 9. Fully optimized B3LYP/6-31++G(2d,2p) structures of the model X-ray Mg^{2+}-binding site with a second-shell carboxylate $\{[MgW_3(HCOO^-)_2\text{-}HCONH_2]\bullet(HCOO^-)\}^-$ (a), Ca^{2+} bound monodentately to three carboxylate groups (b), and Ca^{2+} bound monodentately to two carboxylates and bidentately to the third (c).

protein cavity, it may not displace Mg^{2+}, as evidenced by the positive ΔG^x ($x = 2, 4, 10$) for reaction 1 (8.9–1.6 kcal/mol; Table 5) and ΔG^2 and ΔG^4 for reaction 3 (8.2 and 1.5 kcal/mol, respectively). *Bidentate* binding to one of the carboxylates (Figure 9c) favors the exchange of Mg^{2+} for Ca^{2+} as the respective free energies become less positive, and if the binding site is not deeply buried (i.e., $\epsilon \geq 4$), the $Mg^{2+} \rightarrow Ca^{2+}$ exchange becomes thermodynamically favorable (ΔG^4 and $\Delta G^{10} = -2.3$ and -6.6 kcal/mol for reaction 2 and -5.2 and -10.9 kcal/mol for reaction 4; Table 5). This implies that Ca^{2+} could replace Mg^{2+} in partially buried protein cavities if it binds to a three-carboxylate binding pocket with at least one of them bound in a *bidentate* fashion.

III. Mg^{2+} Binding to "Site" 1 versus "Site" 2. To assess the affinity of the two binding sites for Mg^{2+}, free energies were evaluated for the following reactions mimicking Mg^{2+} binding to "site" 1 (eq 6) and "site" 2 (eq 7):

$$[Mg(H_2O)_6]^{2+} + 2HCOO^- + HCONH_2 \leftrightarrow$$
$$[Mg(H_2O)_3(HCOO^-)_2HCONH_2]^0 + 3H_2O \quad (6)$$

$$[Mg(H_2O)_6]^{2+} + 3HCOO^- \leftrightarrow$$
$$[Mg(H_2O)_2(HCOO^-)_2HC\tilde{O}\tilde{O}]^- + 4H_2O \quad (7)$$

Two of the formates in $[Mg(H_2O)_2(HCOO^-)_2HC\tilde{O}\tilde{O}]^-$ (eq 7) are monodentately bound to Mg^{2+}, while the third one is bidentately coordinated to the metal. The binding free energies for eqs 6 and 7 are given in Table 6.

The gas-phase free energy, ΔG^1, for Mg^{2+} binding to "site" 1 (eq 6) or "site" 2 (eq 7) is dictated by the reaction enthalpy, which is large and negative (Table 6). Not surprisingly, the ΔH^1 for "site" 2 is more negative (by 25 kcal/mol) than that for "site" 1 due to the additional electrostatic interactions with the D70 carboxylate, which is absent in "site" 1 (compare dashed and solid Mg^{2+} curves in Figure 5b). Increasing solvent exposure of the metal-binding site decreases the magnitude of the binding free energy, indicating that a high dielectric environment disfavors Mg^{2+} binding to carboxylate groups. Nevertheless, the ΔG^x ($x = 2, 4, 10$) for "sites" 1 and 2 remain large and

negative, implying that both reactions (eqs 6 and 7) are thermodynamically favorable in deeply buried cavities or partially solvent accessible binding sites. Furthermore, the ΔG^x ($x = 2, 4,$ and 10) values for "site" 2 are more negative than those for "site" 1 (by 10–23 kcal/mol), implying that Mg^{2+} binding at "site" 2 is thermodynamically more preferable than that at "site" 1 if both "sites" have similar solvent accessibility and are characterized by the *same* dielectric constant ϵ.

However, both X-ray and MD structures reveal that "site" 1 is more buried than "site" 2. Based on the two RNase H1 X-ray structures (PDB entries 1RDD and 2RN2), the solvent accessible surface area for "site" 1 is 9–11%, while that for "site" 2 is twice as large, 19–20%. These findings are in line with those from the MD simulations, which also show that "site" 2 is more solvent accessible than "site" 1. The ion–O(water) radial distribution functions in the second shell for Mg^{2+} and Ca^{2+} ions binding at "site" 1 (solid curves, Figure 10) and "site" 2 (dashed curves, Figure 10) show that the second-shell water molecules are closer to the ion and are more structured in "site" 2 as compared to "site" 1.

Since "site" 1 is less solvent accessible than "site" 2, it should be characterized by a smaller ϵ than "site" 2; that is, ϵ("site" 1) $< \epsilon$("site" 2). Assuming that $\epsilon = 2$ for "site" 1 and $\epsilon = 4$ for "site" 2, ΔG^2 for "site" 1 (-155 kcal/mol) is more favorable than ΔG^4 for "site" 2 (-89 kcal/mol). The same trend is obtained if $\epsilon = 4$ for "site" 1 and $\epsilon = 10$ for "site" 2: ΔG^4 for "site" 1 (-72 kcal/mol) is more negative than ΔG^{10} for "site" 2 (-25 kcal/mol). This implies that Mg^{2+} binding at "site" 1 (the buried X-ray-binding site) is thermodynamically more preferable than that at "site" 2, which is more solvent accessible with a greater dielectric constant than "site" 1.

Discussion

Validation of the Predicted Metal-Binding Sites. The finding that Mg^{2+} prefers to bind at "site" 1 while Ca^{2+} prefers to bind at "site" 2 appears to be consistent with available experimental data. The average MD structure of the Mg^{2+}-binding site (Figure 3a) is similar to the respective X-ray structure (Figure 1), except that the weak Mg^{2+}–O(G11) interaction in the low-resolution (2.8 Å) crystal structure is lost during the simulation. However, a high-resolution (1.7 Å) crystal structure of avian sarcoma virus integrase, whose folding topology and active-site geometry are similar to those of RNase H1,[62] shows Mg^{2+} bound monodentately to two carboxylate oxygen atoms and four water molecules, as in the MD simulations (Figure 3a). Furthermore, the DFT/CDM calculations show that the Mg^{2+}–O(G11) interaction does not appear to affect the stability of the metal complex, as evidenced by the similar formation free energies of the Mg^{2+} complex with and without the G11 backbone coordination: the ΔG^1, ΔG^2, $\Delta G,^4$ and ΔG^{10} for forming the "X-ray" Mg^{2+}-binding site, $[Mg(H_2O)_6]^{2+} + 2(HCOO)^- + HCONH_2 \rightarrow [Mg(H_2O)_3(HCOO^-)_2HCONH_2]^0 + 3H_2O$, differ from those for forming the respective "simulation" site, $[Mg(H_2O)_6]^{2+} + 2(HCOO)^- \rightarrow [Mg(H_2O)_4(HCOO^-)_2]^0 + 2H_2O$, by ≤ 2.0 kcal/mol.

Although no three-dimensional structures of RNase H1 or homologous proteins bound to Ca^{2+} are available, the predicted Ca^{2+}-binding site can be indirectly validated by its ability to

(62) Bujacz, G.; Jaskolski, M.; Alexandratos, J.; Wlodawer, A.; Merkel, G.; Katz, R. A.; Skalka, A. M. *Structure* **1995**, *4*, 89.

Table 5. Enthalpies (ΔH^1) and Free Energies (ΔG^x) (in kcal/mol) of Exchanging Mg^{2+} in the X-ray Binding Site for Ca^{2+} Bound in "Site" 2[a]

reaction	ΔH^1	ΔG^1	ΔG^2	ΔG^4	ΔG^{10}
$\{[MgW_3(HCOO^-)_2HCONH_2]\bullet HCOO\}^- + [CaW_7]^{2+} \rightarrow [CaW_4(HCOO^-)_3]^- + [MgW_6]^{2+} + HCONH_2$	21.9	17.2	8.9	4.5	1.6
$\{[MgW_3(HCOO^-)_2HCONH_2]\bullet HCOO\}^- + [CaW_7]^{2+} \rightarrow [CaW_3(HCOO^-)_2(HC\tilde{O}\tilde{O}^-)]^- + [MgW_6]^{2+} + HCONH_2 + W$	28.8	13.9	3.7	−2.3	−6.6
$\{[MgW_3(HCOO^-)_2HCONH_2]\bullet HCOO\}^- + [CaW_8]^{2+} \rightarrow [CaW_4(HCOO^-)_3]^- + [MgW_6]^{2+} + HCONH_2 + W$	34.0	20.2	8.2	1.5	−2.8
$\{[MgW_3(HCOO^-)_2HCONH_2]\bullet HCOO\}^- + [CaW_8]^{2+} \rightarrow [CaW_3(HCOO^-)_2(HC\tilde{O}\tilde{O}^-)]^- + [MgW_6]^{2+} + HCONH_2 + 2W$	40.8	17.0	3.1	−5.2	−10.9

[a] See footnotes to Table 4.

Table 6. Enthalpies (ΔH^1) and Free Energies (ΔG^x) (in kcal/mol) for Mg^{2+} Binding to "Site" 1 and "Site" 2[a]

"site"	reaction	ΔH^1	ΔG^1	ΔG^2	ΔG^4	ΔG^{10}
1	$[MgW_6]^{2+} + 2HCOO^- + HCONH_2 \rightarrow [MgW_3(HCOO^-)_2HCONH_2]^0 + 3W$	−322.8	−319.2	−154.7	−71.6	−14.6
2	$[MgW_6]^{2+} + 3HCOO^- \rightarrow [MgW_2(HCOO^-)_2HC\tilde{O}\tilde{O}]^- + 4W$	−348.1	−354.3	−177.9	−88.9	−25.0

[a] See footnotes to Table 4.
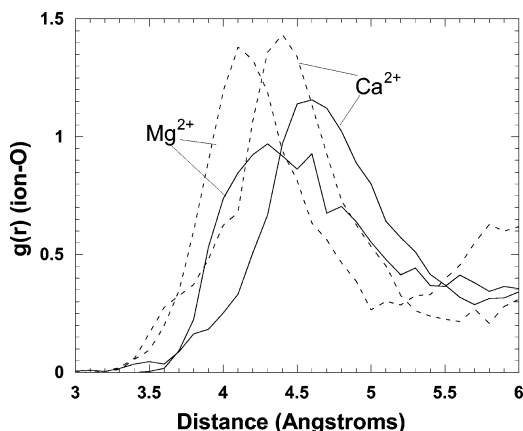
Figure 10. Ion−O(water) radial distribution function in the second shell for Mg^{2+} and Ca^{2+} ions binding at "site" 1 (solid curves) and "site" 2 (dashed curves).

yield the trend of the experimental binding free energies. Both the simulation and DFT/CDM binding free energy trends agree qualitatively with the experimental trend only if Ca^{2+} binds at "site" 2, while Mg^{2+} binds at "site" 1 (Figure 7). On the other hand, if both ions bind at the same site ("site" 1 or "site" 2), then the binding free energy of Mg^{2+} becomes more favorable than that of Ca^{2+}, in contrast to the experimental findings (Figure 6).

Why Mg^{2+} Prefers "Site" 1 to "Site" 2. Mg^{2+} is expected to bind more tightly to "site" 2 due to the stronger interaction with the D70 carboxylate, which is absent in "site" 1 (compare Figures 3a and 4a and Mg^{2+} curves in Figure 5b). This would indeed be the case if "site" 2 and "site" 1 have similar solvent accessibility (Table 6); that is, if $\epsilon("site" 2) = \epsilon("site" 1)$. However, both X-ray and MD structures reveal that "site" 2 is more solvent accessible than "site" 1; that is, $\epsilon("site" 2) > \epsilon("site" 1)$. The higher solvent accessibility of "site" 2 relative to "site" 1 disfavors Mg^{2+} binding to the carboxylates (see above); hence Mg^{2+} prefers "site" 1 to "site" 2 (ΔG^2 or ΔG^4 for "site" 1 is more negative than ΔG^4 or ΔG^{10} for "site" 2, respectively, in Table 6).

Why Ca^{2+} Binds Tighter than Mg^{2+} to RNase H1. The preference of Mg^{2+} for "site" 1 and Ca^{2+} for "site" 2 is probably the result of the delicate balance between metal−water and metal−protein interactions. Solvation effects *favor* Ca^{2+} binding to the protein as the cost of removing first-shell water molecules from Ca^{2+} is significantly less than that from Mg^{2+}, whose hydration free energy is more favorable than the Ca^{2+} hydration

free energy (by ∼74 kcal/mol, see Table 2). On the other hand, amino acid interactions *disfavor* Ca^{2+} binding to the protein, as they are weaker with Ca^{2+} than with Mg^{2+}. Therefore, if Mg^{2+} and Ca^{2+} bind at the same site ("site" 1) by replacing two first-shell water molecules with D10 and E48, Ca^{2+} is found to bind to RNase H1 more weakly than Mg^{2+} because its smaller desolvation penalty ($\Delta\Delta G_{solv}^{aq} (Mg^{2+}-Ca^{2+}) = -75.6 \pm 0.1$ kcal/mol) is outweighed by weaker $Ca^{2+}-O$ interactions ($\Delta\Delta G_{solv}^{prot} (Mg^{2+}-Ca^{2+}) = -86.5 \pm 1.4$ kcal/mol); hence, from eq 1, $\Delta G^{Ca} - \Delta G^{Mg} = \Delta\Delta G_{solv}^{aq} - \Delta\Delta G_{solv}^{prot}$ is positive (10.9 kcal/mol). However, if Ca^{2+} binds instead to "site" 2 where it gains two $Ca^{2+}-O(D70)$ interactions at the expense of two weaker $Ca^{2+}-O(water)$ ones, $\Delta\Delta G_{solv}^{prot}(Mg^{2+}-Ca^{2+})$ becomes less negative (-70.5 ± 1.4 kcal/mol), thus allowing Ca^{2+} to bind to the enzyme more tightly than Mg^{2+}; that is, $\Delta G^{Ca} - \Delta G^{Mg} = \Delta\Delta G_{solv}^{aq} - \Delta\Delta G_{solv}^{prot}$ becomes negative (-5.1 kcal/mol). As Ca^{2+} binds to D10 in β-strand 1, E48 in helix A, and D70 at the C-terminus of helix B, it could stabilize these three secondary structural elements, whereas Mg^{2+} would stabilize only $\beta1$ and αA (see Figure 1).

How RNase H1 Selects Mg^{2+} over Ca^{2+} When It Binds Ca^{2+} Tighter than Mg^{2+}. The metal exchange free energy, $\Delta\Delta G^{ex}$ ($= \Delta G^{Ca} - \Delta G^{Mg}$), for Mg•RNase + Ca(II) → Ca•RNase + Mg(II) can be related to the concentrations of the free metal cations:

$$\Delta\Delta G^{ex} = -2.303RT \log \frac{[Ca\bullet RNase][Mg]}{[Mg\bullet RNase][Ca]}$$

$$\approx -2.303RT \log\frac{[Mg]}{[Ca]} \quad (8)$$

where the concentrations of Mg^{2+}- and Ca^{2+}-bound RNase H1 are assumed to be similar. Solving this equation for a $\Delta\Delta G^{ex}$ of -2.2 kcal/mol, evaluated from our in vitro experiments (see Table 3), yields $[Mg^{2+}]/[Ca^{2+}] \approx 10^{1.6}$. This implies that Ca^{2+} can replace Mg^{2+} from the RNase H1 binding site if its concentration is no more than 2 orders of magnitude less than the concentration of Mg^{2+}. However, the in vivo $[Mg^{2+}]/[Ca^{2+}]$ ratio is 10^4 in favor of Mg^{2+} as the concentration of free Mg^{2+} in the cell is $10^{-3}-10^{-4}$ M,[63] while that of free Ca^{2+} is $10^{-7}-10^{-8}$ M.[64−66] Note that the physiological $[Mg^{2+}]$ is of the same

(63) Romani, A.; Scarpa, A. *Arch. Biochem. Biophys.* **1992**, *298*, 1.
(64) Niki, I.; Yokokura, H.; Sudo, T.; Kato, M.; Hidaka, H. *J. Biochem.* **1996**, *120*, 685.
(65) Berridge, M. J.; Bootman, M. D.; Lipp, P. *Nature* **1998**, *395*, 645.
(66) Ikura, M. *Trends Biochem. Sci.* **1996**, *21*, 14.

order of magnitude as the concentration at which Mg^{2+} activates the RNase H1 (0.5−5 mM). Thus, even though RNase H1 could bind Ca^{2+} tighter than Mg^{2+}, it selects Mg^{2+} over Ca^{2+} in vivo probably due to the natural abundance of Mg^{2+} relative to Ca^{2+} in the cell.[67,68]

Why Ca^{2+} Inhibits Enzyme Activity But Mg^{2+} Does Not. The invariant D70 has been postulated to play a critical role in RNase H1 catalysis by acting as a general base.[18] In "site" 1, Mg^{2+} binds to four water molecules, which prevents D70 from binding directly to Mg^{2+}, allowing D70 to activate a water molecule for subsequent attack at the phosphorus atom. In other words, Mg^{2+} promotes general base catalysis by an outer-sphere mechanism.[69] On the other hand, Ca^{2+} binds at "site" 2 to both carboxylate oxygen atoms of D70, which prevents D70 from acting as a general base. Note that if Ca^{2+} were to bind monodentately to D70, the free D70 carboxylate oxygen might still activate a water molecule. This shows how the mode of carboxylate binding to a metal ion could affect catalysis. These theoretical findings in conjunction with the enzyme activity and site directed mutagenesis data, in turn, implicate a crucial role for D70 as a general base in RNase H1 catalysis.

Why Ba^{2+} and Sr^{2+} Bind RNase H1 with Affinity Similar to That of Mg^{2+} but Abolish Enzyme Activity. For Sr^{2+} and Ba^{2+}, both experimental and theoretical data suggest that they bind at "site" 1 to D10 and E48, as for Mg^{2+}. The experimental binding enthalpy and entropy of Sr^{2+} and Ba^{2+} are similar in magnitude and sign to those measured for Mg^{2+} (see Table 3). The similar thermodynamic parameters obtained for Sr^{2+}, Ba^{2+}, and Mg^{2+} could be rationalized by the weaker Sr^{2+}/Ba^{2+}− O(carboxylate) interactions relative to Mg^{2+} (compare solid curves for Sr^{2+}, Ba^{2+}, and Mg^{2+} in Figure 5b) being largely compensated by the smaller cost of removing first-shell water molecules from Sr^{2+} or Ba^{2+} compared to Mg^{2+} (Table 2). However, if Sr^{2+} or Ba^{2+} were to bind at "site" 2 where relative to "site" 1 it gains three protein interactions (one with D10 and two with D70, see Figure 4c), its binding enthalpy would be significantly more negative than the Mg^{2+} binding enthalpy, as evidenced by the deeper potential well at Sr^{2+} and Ba^{2+} in "site" 2 (Figure 5b, dashed curve) compared to the potential well at Mg^{2+} in "site" 1 (Figure 5b, solid curve). Furthermore, the free energy of Sr^{2+} binding to "site" 1 relative to that of Ca^{2+} from free energy simulations (2.1 kcal/mol) is very close to the respective experimental number (2.5 kcal/mol, Table 3).

Although in "site" 1, Sr^{2+}/Ba^{2+} does not coordinate to D70, its larger first coordination sphere and greater number of loosely bound water molecules compared to Mg^{2+} could either affect the activation of water by D70 or obstruct the substrate binding and hence enzyme activity. The binding mode of Ba^{2+} and Sr^{2+} could be verified by measuring the unfolding rate of the $Mg^{2+}/$ $Ca^{2+}/Sr^{2+}/Ba^{2+}$-bound RNase H1. An unfolding rate of the $Sr^{2+}/$ Ba^{2+}-bound RNase H1 that is faster than the Ca^{2+}-bound enzyme, but similar to that of the Mg^{2+}-bound enzyme, would suggest that Sr^{2+} and Ba^{2+}, like Mg^{2+}, binds at "site" 1.[24]

Factors Governing the Free Energy Profile as a Function of the Born Radius. The calculations also suggest the factors governing the shape of the free energy profile as a function of the Born radius. An increase in the binding free energy with increasing Born radius, as shown by the solid and dashed curves in Figure 6, suggests a similar binding site for each metal. In this case, the binding free energy becomes less favorable with increasing size of the metal due to weaker ion−ligand interactions (Figure 5b). On the other hand, a V-shaped binding free energy profile with increasing Born radius, as shown by the dotted curve in Figure 6, reflects a change in the ligand coordination of the metal around the free energy minimum. In the case of RNase H1, the larger Ca^{2+} binds more tightly to the enzyme than Mg^{2+} because it coordinates not only to the ligands of the smaller Mg^{2+} but also gains additional interactions by forming bidentate interactions with D70. The trend in binding free energies also reflects the different water affinities of each metal ion: Mg^{2+} prefers to bind to the protein with as many as four water molecules, whereas Ca^{2+} prefers to bind to carboxylate groups in bidentate/monodentate fashion with a depleted water shell.

(67) Dudev, T.; Lim, C. *J. Phys. Chem. B* **2001**, *105*, 4446.
(68) Dudev, T.; Lim, C. *Chem. Rev.* **2003**, *103*, 773.
(69) Jou, R.; Cowan, J. A. *J. Am. Chem. Soc.* **1991**, *113*, 668.